Resistance welding of NiTi SMA tubes

V. Delobelle[(1)], P. Delobelle[(2)], Y. Liu [(3)], D. Favier[(1)*], H. Louche[(4)],

* : Corresponding author : D.Favier

[(1)] Université de Grenoble, CNRS, Laboratoire 3SR, B.P. 53, F-38041 Grenoble Cedex 9, France.

Phone : +33 (0)4 76 82 70 42, Fax : +33 (0)4 76 82 70 43.mei

eMail : denis.favier@grenoble-inp.fr

[(2)] Laboratoire de mécanique appliquée, Femto, 24 Rue de l'épitaphe, 25000 Besançon – France.

Phone : +33 (0)3 81 66 60 13, Fax : +33 (0)3 81 66 67 00.

eMail : patrick.delobelle@univ-fcomte.fr

[(3)] School of Mechanical and Chemical Engineering, The University of Western Australia, 35 Stirling Highway, Crawley, WA 6009, Australia.

Phone : +61 (0)8 64 88 31 32, Fax : +61 (0)8 64 88 10 24

eMail : yinong.liu@uwa.edu.au

[(4)] Laboratoire de Mécanique et de Génie-Civil (LMGC), Université Montpellier 2, CNRS, CC 048, Place Eugène Bataillon, 34095 Montpellier Cedex - France.

Phone : +33 (0)4 67 14 96 34, Fax : +33 (0)4 50 09 66 49.

eMail : herve.louche@univ-montp2.fr

Abstract:

Resistance welding is studied as a technique to join NiTi shape memory alloy thin-walled tubes. Properties of the welded metal are compared to those of the base metal by means of differential scanning calorimetry measurements, microstructure observations and nanoindentation tests. The effect of post-welding thermomechanical treatment is studied. Strength of the joint is analyzed by means of tensile and compression tests performed on as welded and heat treated tubes.

Key words: Resistance welding, NiTi shape memory alloy, martensitic phase transformation, superelasticity, mechanical properties.

1. Introduction

For many years engineers have used the unique properties of NiTi shape memory alloy (SMA), such as superelasticity and shape memory effect associated with the reversible B2-B19' martensitic transformation, to design and create new and sophisticated products. Owing to its good biocompatibility, NiTi has been used in various biomedical applications, such as those mentioned in Duerig et al. (1999), such as vascular stents, endodontic drills or endoscopic instruments, atrial septal occlusion device, etc. Various forms of NiTi have also been combined with other materials to create new intelligent composites and structures, e.g., Liu et al. (2008) realized composites composed of ferroelectric ceramics deposited on NiTi films by the sol-gel method, Chen et al. (2009) built composite tube reinforced with shape memory alloys or Zhao et al. (2006) realized an absorbing system composed of a spring and porous NiTi.

Bansidhi et al. (2008) proposed an overview of the strong interest of NiTi powders as precursor materials for the creation of bio-compatible porous implants. Different ways to produce these cellular structure are used such as self-propagating high temperature synthesis (SHS) described by Chu et al. (2004), selective laser sintering described by Shishkovsky et al. (2009), spark-plasma sintering (SPS) described by Ye et al. (1998), hot isostatic pressing (HIP) described by Mentz et al. (2008) or capsule-free hot isostatic pressing (CF-HIP) described by Wu et al. (2007) for examples. However, the pore structure (pore size, shape, and direction) cannot be controlled effectively using these methods.

More recently, efforts have also been made to create various materials architectures to further enhance the functionality of SMAs by combining their unique properties with designed materials structures. Pilch et al. (2009) used Thin NiTi wires to create NiTi superelastic textiles. These textiles would have different properties considering stitch. They can be thermally actuated and are shapeable. In the biomedical fields, they can be used as superelastic cell growth scaffolds. In 2007, Shaw et al. (2007) created superelastic NiTi honeycombe structures, allowing a maximum recoverable deformation of 50% by combining structural effects and the superelasticity of NiTi. These kinds of cellular materials would be an interesting alternative to porous NiTi, with controlled pore structure.

To create the various materials architectures of SMAs, various materials fabrication and joining techniques have been studied. The honeycomb structure presented by Grummon et al. (2006) was created by brazing pre-shaped NiTi plates using niobium. Gugel et al. (2008), for example, studied laser welding to join NiTi wires. This study shows that the created NiTi/NiTi joints reach about 75% of the ultimate tensile strength of pure NiTi. Other techniques, such as adhesive bonding, realized by laser nitriding process, described by Man

and Zhao (2006) and explosive welding described by Yan et al. (2007) have also been tested. Akselen (2010) provided a good overview of the common techniques studied to join NiTi sheets. In comparison, few studies have been reported on resistance welding of NiTi as the one proposed by Nishikawa et al. (1983) on NiTi wires. This study shows that tensile strength of the welded wire is about 80%. This result is close to the one obtained by Gugel et al. previously presented. Tam et al. (2012) also studied resistance welding of NiTi wires, and shows the impact of the electrical delivered intensity. It shows that only one specific value allow to obtain the higher joint breaking force.

This paper reports a study on electrical resistance welding to join NiTi tubes. This method is studied in view to establish a technique for the design and creation of self-joined NiTi material architectures from stacked tubes.

2. Experimental details

A superelastic Ti-50.8 at. % Ni tubing material supplied by Minitubes SA (Grenoble - France) was used. The tube has an outer diameter of $Ø_{ext}$=7 mm and a wall thickness of 0.2 mm. For resistance welding, tubular samples of L = 5 mm length were cut. Oxide surface layer was removed with abrasive paper to improve electrical contact at the joint.

A DC Hughes Model VTA-60 resistance welder was used. Welding set-up is illustrated in Fig. 1. The electrodes were approximately 20 mm long plates sharpened at the edge, to allow welding along a contact line. Resistance welding was made using an electrical pulse energy of E = 50 J and a contact force of F = 18 N. Each weld was done in 5 repeated pulses. Some welded samples were heat treated after welding. These samples were first solution treated at

850°C for one hour in Argon atmosphere and then aged at 450°C for 30 minutes. The transformation behaviour of the initial material and of the joint is studied using a differential scanning calorimeter (TA Q20) at 10 K min^{-1}, in as welded and heat treated conditions.

The microstructure of the samples was examined using a Zeiss 1555 field emission scanning electron microscope (SEM). Mechanical properties of the alloy in the welded zone were studied by means of nanoindentation (nano-indenter II^S) at room temperature using a Berkovich type indenter. The test was conducted following the continuous contact stiffness measurement procedure proposed by Olivier and Pharr (1992) with a frequency of 45 Hz and an indenter vibration amplitude of 1 nm. The maximum penetration depth h_{max} was 1200 nm with a penetration speed of 20 nm s^{-1}.

Mechanical properties of the joined tubes were characterized in both radial compression and tension using a Gabo Explexor instrument at 40°C. To conduct tensile testing of the joined tubes, a special device was developed, as shown in Fig. 2. The two cylindrical pins with outside diameter equal to the inner diameter of the tubes are inserted in the tubes. Tensile loading is then applied to these pins.

3. Results and discussion

3.1. Joint microstructure

Fig. 3 shows microstructure of two welded samples. Fig. 3.a shows the microstructure of the welded section of a sample. The section may be divided into two zones, including the fusion zone, which is about 200 µm in width, and the unaffected base metal. The joint is formed

within the fusion zone. Fig. 3.b. shows the unaffected zone at a higher magnification. It contains small equiaxial grains and the average grain size is ~8 µm. Fig. 3.c shows the fusion zone at a higher magnification. The fusion zone is composed of columnar grains oriented in the tube wall thickness direction, consistent with the direction of the maximum heat dissipation. The biggest grains are approximately 100 µm long and ~20 µm in width.

Fig. 3.d shows the microstructure of a heat treated (solution treatment and ageing) sample. The fusion zone contains large grains. The shape and size remain almost identical to those in the as-welded sample. Fig. 3.e shows the unaffected zone at a higher magnification. It is evident that the equiaxial grains in the base metal have grown to 20-30 µm, more than twice the sizes of the grains before the heat treatment.

3.2. Transformation behaviour

Fig. 4 shows the transformation behaviour of two samples. Sample (a) was in solution treated state. It exhibits a single-stage transformation between the austenite (A) and the martensite (M), with T_s^{A-M} = -20°C, T_f^{A-M} = -70°C, T_s^{M-A} = -25°C and T_f^{M-A} = 10°C. After ageing at 450°C (sample (b)), the R phase appears on both cooling and heating.

Fig. 5 shows the transformation behaviour of three welded samples. For each sample, two DSC specimens were taken, one from the joint (blue curves) and the other from the unaffected initial metal (red curves), as schematically illustrated in Fig. 5.a.

Fig. 5.b shows the transformation behaviour of an as-welded sample. The initial material (red curve) shows no transformation peak. The joint material (blue curve) exhibits a single-stage

A-M transformation, with T_s^{A-M} = -20°C, T_f^{A-M} = -70°C, T_s^{M-A} = -25°C and T_f^{M-A} = 10°C. The transformation temperatures are similar to those of the solution treated sample (Fig. 4, red curve).

Fig. 5.c shows the transformation behaviour of a welded sample after solution treatment. It is seen that the joint and the initial materials show similar transformation behaviours after the solution treatment. As scheduled, the welded sample after solution treatment exhibits identical transformation as the solution treated initial material.

Fig. 5.d shows the transformation behaviour of a sample subjected to welding, solution treatment and ageing at 450°C for 30 minutes. The joint specimen and the initial metal both show A→R→M transformations on cooling and heating. The starting and finishing temperatures of transformations are different. Considering the effect of ageing on the transformation behaviour of Ti - 50.9 at. %Ni proposed in Zheng et al. (2008), the solution treated and aged initial material exhibit a transformation behaviour similar to the one obtained after ageing at 430-460°C and that of the joint material similar to the one obtained after ageing at 460-490°C.

Thus, if the solution treatment seems to homogenize the complete transformation behaviour of the structure, the ageing treatment restores a relative heterogeneous structure.

3.3. Joint micromechanical properties

Nanoindentation measurements were performed at different points along the joint. The distance of these points to the middle of the joint is noted *d*, as shown in Fig. 6.a. Fig 6.b

shows the representative indentation curve (mean over 10 indentations). The experiments were conducted at room temperature, with the testing temperature being approached by heating from below 0°C. As seen in Fig. 5.b, both the weld and base materials are fully austenitic at 20°C before heat treatment. The heat treated samples (Fig. 5.d) are a mixture of martensite and R-phase at this temperature, with a lower martensite fraction for the joint material.

Fig. 6.b shows two indentation curves from an as-welded sample and two others from a heat treated sample. Curve (1) is an as-welded sample, tested at d=0 mm, corresponding to the joint material at the joint centre. Curve (2) is of the same sample as curve (1) but tested at d=1.5 mm, far enough from the joint to be in the unaffected zone. Curves (3) and (4) are of a sample heat treated after welding, tested at d=0 and d=1.5 mm, respectively. It is seen that for the as-welded sample, the stiffness of the joint (curve 2) is lower than that of the initial material (curve 1), while the remnant depth after indentation is higher for the joint material than for the initial material. For the heat treated sample, the stiffness of the initial material (curve 4) is slightly higher than that of the joint (curve 3). This is attributed to the higher initial martensite fraction for the initial material (see Fig. 5.d). The remnant depths are similar between the two locations.

Fig. 7 shows the hardness variation along distance d. Curve 1 (red curve) is obtained from a sample in the as-welded state. Curve 2 (blue curve) is for a sample heat treated after welding. Each H_B value shown in the figure is the average of 10 indentation measurements conducted at the d position over an area of 200 x 200 μm^2 (d ± 100 µm - horizontal line) for an indentation depth comprised between 850 and 1200 nm. The mean scattering is about ±0.7 GPa and ±0.4 GPa for the as-welded and heat-treated samples, respectively. The difference in

data scattering margin is attributed to differences in sample preparation (e.g., polishing) as described in Qasmi and Delobelle (2006).

It is seen that the hardness of the joint material in the as-welded sample (H_B^{joint}= 2.9 ±0.5 GPa) is considerably lower than that of the initial material (H_B^{tubs} = 5.4 ± 0.9 GPa). The variation of H_B with *d* can be divided into three distinct zones: the joint, the heat affected zone where the hardness increases and initial materials with a constant hardness, as indicated in the figure. As seen in the micrograph, the joint zone is within *d* ≈ ±0.1 mm, smaller than the range identified by the nanohardness measurement (*d* ≈ 0.3 mm). Thus, mechanically the heat affected zone is bigger than the fusion zone observed to SEM. Hardness of the heat treated sample (curve 2 – blue curve) shows that the hardness of the joint material remains unchanged with heat treatment (H_B^{joint} = 2.9 ± 0.4 GPa), while hardness of the initial material is reduced to H_B^{tubs}= 2.5 ± 0.5 GPa.

Fig. 8.a shows the evolution of elastic moduli of as-welded samples with indentation depth at different d locations (*d*=0, 0.75, 1 and 1.5 mm). For each curve, each point is the mean value of 10 tests performed over an area of 200 x 200 µm^2 (*d* ± 100 µm-horizontal line) relatively to the *d* value. Dispersions of these measurements are shown in Fig. 8.b. Similarly, the elastic moduli determined at different penetration depth and the scattering of the data for a heat treated sample are shown in Fig. 8.c and Fig. 8.d, respectively.

The modulus of the initial material (*d*=1.5 mm) shows a strong decrease with the indentation depth. This is due to the increased stress-induced martensitic transformation at the indenter tip as experimentally observed in Moyne et al. (1999) and numerically studied in Muir Wood and Clyne (2006). In this regard, modulus values determined at low indentation depths are closer

to the true value of the Young's modulus of the austenite. Thus, the Young's modulus of the austenite is determined to be E_A = 88 ± 9 GPa by extrapolating the curve to h = 0, while Moyne et al. (1999) measured a higher elastic moduli by nanoindenation with E_A = 116 ± 15 GPa, and Liu and Xiang (1998) measured E_A = 35 GPa from classical stress-strain curves. For d = 0 and d = 0.75 mm, the modulus is practically unchanged over the indentation depth range and equal to E = 68 ± 8 GPa. These observations suggest that the joint material is probably not superelastic. This is consistent with the expectation that the joint is similar to solution treated material (Fig. 5.b), which does not exhibit good superelastic behaviour at room temperature as observed with an identical material by Jiang et al. (2009).

The elastic modulus of the heat-treated sample is nearly constant over the indentation depth range, at E = 67 ± 8 GPa. This value is similar to the elastic modulus of the joint material before heat treatment. This implies that heat treatment does not affect the mechanical properties of the joint but only those of the initial material. This is consistent with DSC observations that the joint material and the initial material after heat treatment show similar transformation behaviour.

Fig. 8.b and Fig. 8.d. show the dispersion of the data with the indentation depth. For the two samples, dispersion is almost equal, constant and inferior to 12 GPa. This value leads to an error of approximately 17% on the Young modulus value.

3.4. Mechanical tests on welded tubes

Fig. 9 shows compression and tension tests realized on as-welded (red curve) and heat treated (blue curve) joined tubes. The tests were conducted in a climatic chamber at 40°C with

crosshead velocities of 2 mm min^{-1} and 0.2 mm min^{-1} for the tension and compression tests, respectively. Tension tests were performed using the device presented in the "Experimental details" section. The compression tests were performed between compression plates. To avoid tube sliding during compression tests, adhesive tape was put between the plates and the samples. The compression strain is defined as $\frac{\Delta L}{2\,\emptyset_{ext}}$ where ΔL is the displacement of the upper moving plate.

Force-strain curves obtained during cyclic compression tests of joined twin-tube samples are plotted in Fig. 9.a. Fig. 9.b shows force-displacement curves during tension tests of joined twin-tube samples conducted until joint rupture. Cyclic compression tests show the superelastic behaviour of the joined tubes at 40°C. During these tests, the welded zone is weakly deformed and does not play an important role on the overall behaviour of the joined tubes. The joined tubes are found to fail mainly by excessive deformation of the material outside the heat affected zone. It is seen that the as-welded joined twin-tube samples are much stiffer than the heat treated samples.

The experimental set-up of the tension test was designed to deform mainly the joint zone. Fig. 9.b shows four loading curves, including two joined twin-tube samples in as-welded state (red curves) and two other samples in heat treated state (blue curves). Round marks indicate joint rupture. It is seen that the as-welded joined twin-tube samples are much stiffer than the heat treated samples. This stiffness difference, also observed during nanoindentation tests and compression tests between the as-welded and heat-treated specimens is thus easily explained considering the transformation behaviour of the initial material as measured by DSC in the as-welded (Fig. 5.b) and heat treated (Fig. 5.d) states.

The measured fracture load values are very scattered, ranging between 20 and 120 N. Considering the best results and a cross section of approximately L x l = 5 x 0.2 mm, where L

is the sample length and l is the width of the joint estimated from SEM micrograph, and a maximum load of 120 N, the joint is able to support a tensile stress of approximately 120 MPa.

4. Conclusions

Analysis of the experimental evidences presented above leads to the following conclusions:

(i) Transformation behaviour, microstructure and mechanical properties of the joint are significantly affected by the welding process. Transformation behaviour of the joint is practically identical to that of Ti-50.8 at% Ni annealed at 850°C. The material is not superelastic under this condition. Grains within the fusion zone of the joint are much bigger than those in the initial material. Hardness of the joint material is 2.9 ± 0.5 GPa and that of the initial material is 5.4 ± 0.9 GPa. The welded structure is highly heterogeneous.

(ii) After solution treatment at 850°C for 60 min followed by ageing at 450°C for 30 min, the transformation behaviour of the joint and of the initial material is almost identical. The heat treatment does not change significantly the grain size, hardness and elastic moduli of the joint. However, the heat treatment increases the average grain size of the initial material and changes its micromechanical properties.

(iii) The weld can support a tensile load of 120 N, corresponding to the tensile stress of 120 MPa. As-welded twin-tube samples are stiffer than heat treated twin-tube samples in both compression and tension.

Given the above, this study demonstrates that resistance welding is a feasible technique for joining NiTi for the design and creation of complex structures with low density and high reversible elasticity.

Acknowledgement

The authors wish to acknowledge the financial support of the ANR research program ANiM: Architectured NiTi Material (N.2010 BLAN 90201). V. Delobelle held a fellowship from la Région Rhône-Alpes (France). Y. Liu acknowledges the experimental support of the Centre for Microscopy, Characterization and Microanalysis of the University of Western Australia for electron microscopy and microstructure analysis.

References

Akselen, O.M., 2010. Joining of shape memory alloys, edited by Corneliu Cismasiu, published by Sciyo. Shape Memory Alloys - Chap. 9.

Bansiddhi, A., Sargeant, T.D., Stupp, S.I., Dunand, D.C., 2008. Porous NiTi for bone implants: A review. Acta Biomater. 4, 773-782.

Chen, H.W., Sun, H.-K., Liu, T.-C., 2009. Autofrettage analysis of a fibre reinforced composite tube structure incorporated with a SMA. Compos. Struct. 89, 497-508.

Chu, C.L., Chung, C.Y., Lin, P.H., Wang, S.D., 2004. Fabrication of porous NiTi shape memory alloy for hard tissue implants by combustion synthesis. Mat. Sci. Eng. A 366, 114-119.

Duerig, T., Pelton, A., Stockel, D., 1999. An overview of nitinol medical applications. Mat. Sci. Eng. A 273-275, 149-160.

Grummon, D.S., Shaw, J.A., Foltz, J., 2006. Fabrication of cellular shape memory alloy materials by reactive eutectic brazing using niobium. Mat. Sci. Eng. A 438-440, 1113-1118.

Gugel, H., Schuermann, A., Theisen, W., 2008. Laser welding of NiTi wires. Mat. Sci. Eng. A 481-482, 668-671.

Jiang, F., Liu, Y., Yang, J.A., Li, L., Zheng, Y., 2009. Effect of ageing treatment on the deformation behaviour of Ti Ni 50.9 at.%. Acta Mater. 57, 4773-4781.

Liu, Q.S., Liu, Y.F., Ma, X., Han, X., 2008. Study of the structure and interface of NiTi SMA/FC composite films prepared by the sol gel method. Mater. Char. 59, 188-191.

Liu, Y., Xiang, H., 1998. Apparent modulus of elasticity of near equiatomic NiTi. J. Alloys Comp. 270, 154-159.

Man, H.C., Zhao, N.Q., 2006. Enhancing the adhesive bonding strength of NiTi shape memory alloys by laser gas nitriding and selective etching. Appl. Surf. Sci. 253, 1595-1600.

Mei, Q.S., Zhang, L., Tsuchiya, K., Gao, H., Ohmura, T., Tsuzaki, K., 2010. Grain size dependence of the elastic modulus in nanostructured NiTi. Scripta Mater. 63, 977-980.

Mentz, J., Bram, M., Buchkremer, H.P., Stover, D., 2008. Influence of heat treatments on the mechanical properties of high-quality Ni-rich NiTi produced by powder metallurgical methods. Mater. Sci. Eng. A 481-482, 630-634.

Moyne, S., Poilane, C., Kitamura, K., Miyazaki, S., Delobelle, P., Lexcellent, C., 1999. Analysis of the thermomechanical behaviour of TiNi shape memory alloy thin films by bulging and nanoindentation procedures. Mater. Sci. Eng. A 273-275, 727-732.

Muir Wood, A.J., Clyne, T.W., 2006. Measurement and modelling of the nanoindentation response of shape memory alloys. Acta Mater. 54, 5607-5615.

Nishikawa, N., Tanaka, H., Kohda, M., Nagaura, T., Watanabe, K., 1982. Behaviour of welded part of Ti-Ni shape memory alloys. J. de Phys. 43, C4, 839-844.

Olivier, W.C., Pharr, G.M., 1992. An improved technique for determining hardness and elastic modulus using load and displacement sensing indentation experiments. J. Mater. Res. 7, 1564-1583.

Pilch, J., Heller, L., Sittner, P., Sept. 7-11 2009. Final thermomechanical treatment of thin NiTi filaments for textile applications by electric current, in The 8th European Symposium on Martensitic Transformations (ESOMAT 2009), Prague, Czech Republic, published by EDP Sciences (2010), DOI. 10. 1051/esomat/200905024.

Qasmi, M., Delobelle, P., 2006. Influence of the average roughness Rms on the precision of the Young's modulus and hardness determination using nanoindentation technique with a Berkovich indenter. Surf. Coat. Tech. 201, 1191-1199.

Shaw, J.A., Grummon, D.S., Foltz, J., 2007. Superelastic NiTi honeycombs: fabrication and experiments. Smart Mater. Struct. 16, 170-178.

Shishkovsky, I., Morozov, Y., Smurov, I., 2009. Nanostructural self-organization under selective laser sintering of exothermic powder mixtures. Appl. Surf. Sci. 255, 5565-5568.

Tam, B., Pequegnat, A., Khan, M.I., Zhou, Y., 2012. Resistance microwelding of Ti-55.8 wt pct Ni Nitinol wires abd the effects of pseudoelasticity. Met. Mat. Trans. A 43, 2969-2978.

Wu, S., Chung, C.Y., Liu, X., Chu, P.K., Ho, J.P.Y., Chu, C.L., Chan, Y.L., Yeung, K.W.K., Lu, W.W., Cheung, K.M.C., Luk, K.D.K., 2007. Pore formation mechanism and characterization of porous NiTi shape memory alloys synthesized by capsule-free hot isostatic pressing. Acta Mater. 55, 3437-3451.

Yan, Z., Cui, L.S., Zheng, Y.J., 2007. Microstructure and martensitic transformation behaviours of explosively welded NiTi/NiTi laminates. Chin. J. of Aeronautics 20, 168-171.

Ye, L.L., Liu, Z.G., Raviprasad, K., Quan, M.X., Umemoto, M., Hu, Z.Q., 1998. Consolidation of amorpous NiTi powders by spark plasma sintering. Mater. Sci. Eng. A 241, 290-293.

Zhao, Y., Taya, M., Izui, H., 2006. Study on energy absorbing composite structure made of concentric NiTi spring and porous NiTi. Int. J. of Solids Struct. 43, 2497-2512.

Zheng, Y., Jiang, F., Li, L., Yang, H., Liu, Y., 2008. Effect of ageing treatment on the transformation behaviour of Ti Ni 50.9 at.%. Acta Mater. 56, 736-745.

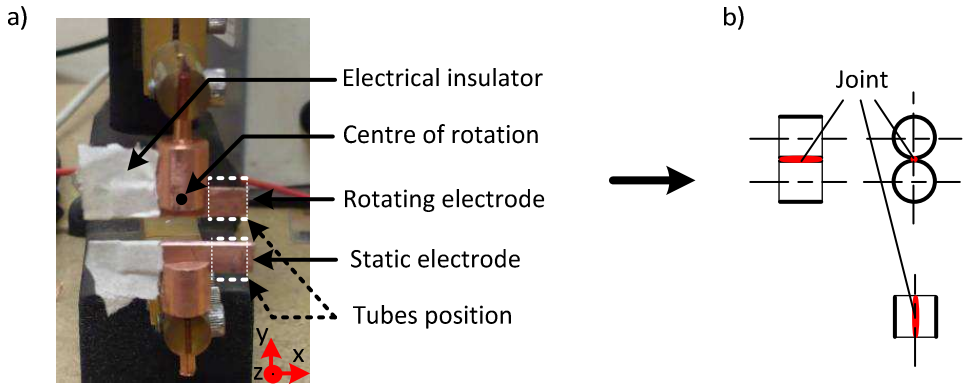

Figure 1: Electrical resistance welding process: (a) welder set-up and (b) schematic of the line weld between tubes.

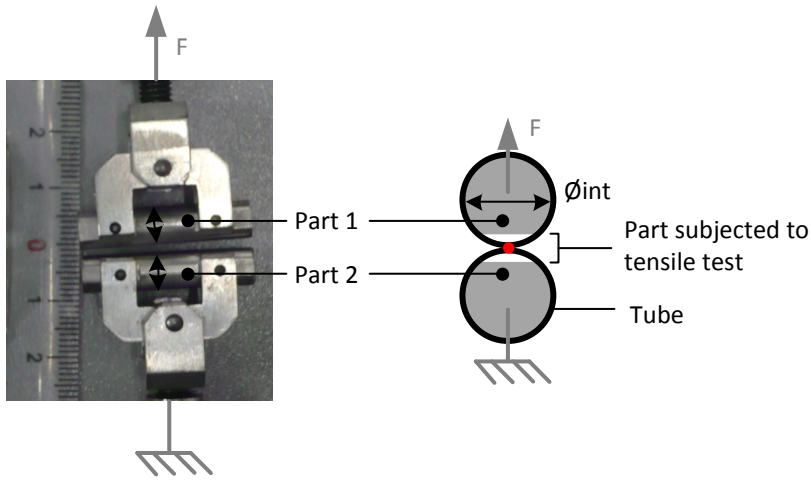

Figure 2: Developed device for tensile testing of strength of the line joint between joined tubes.

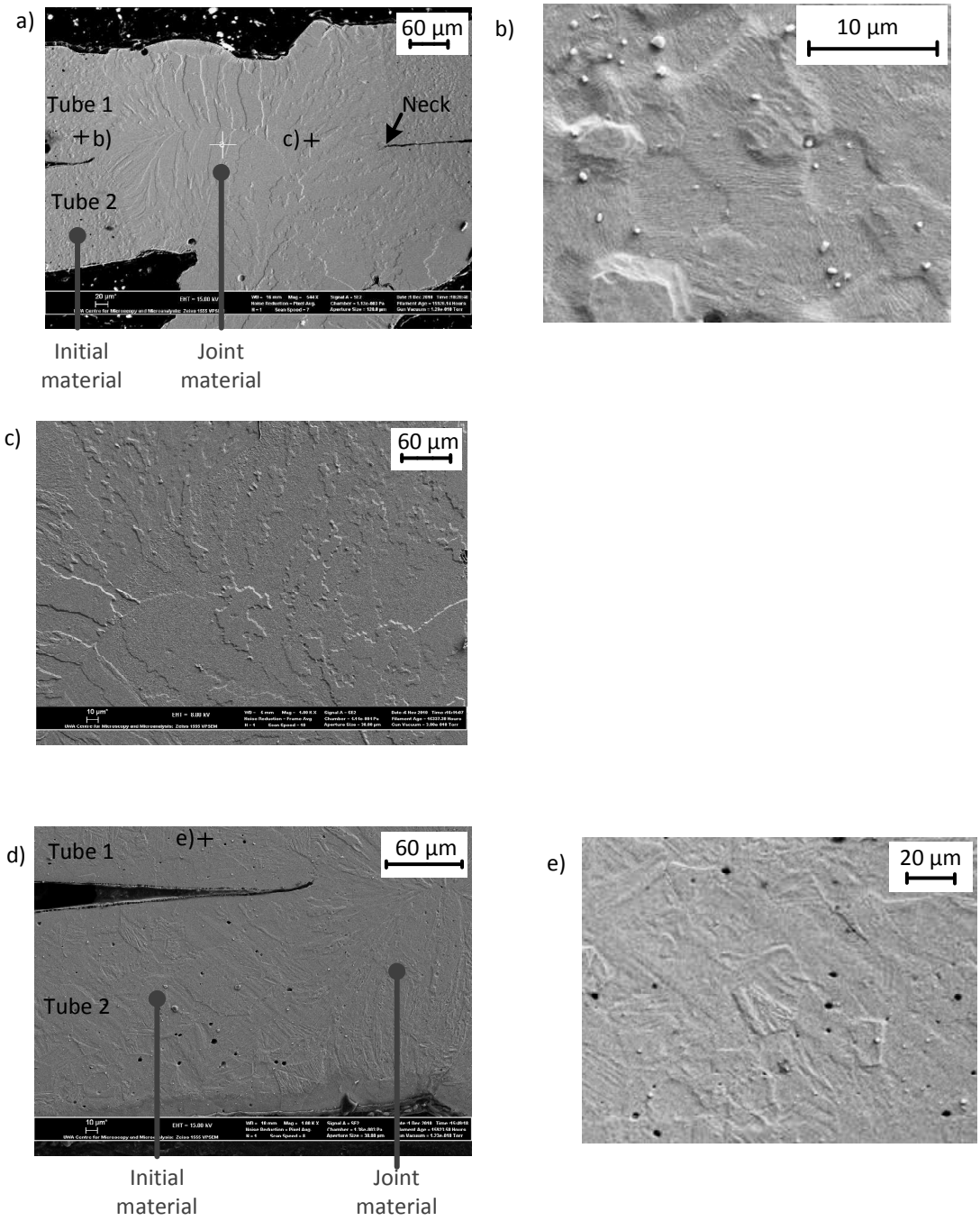

Figure 3: Micrographs of welded sample: (a) full joint, (b) initial material and (c) joint metal. Micrograph of heat treated sample: (d) full joint and (b) initial material.

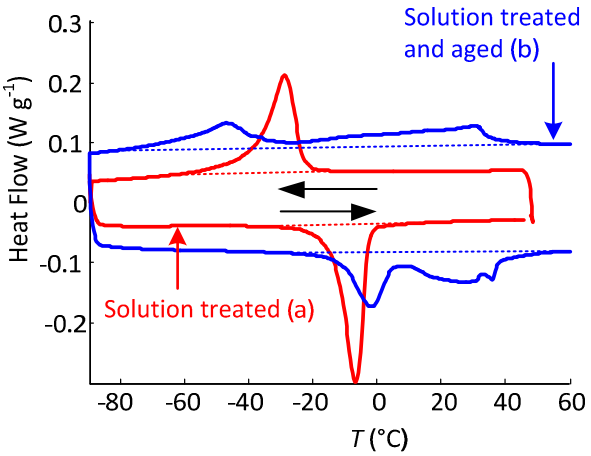

Figure 4: Transformation behaviour of Ti-50.8 at.% Ni tube sample in solution treated (Sample (a)) and solution treated with 450°C aged (sample (b)) conditions.

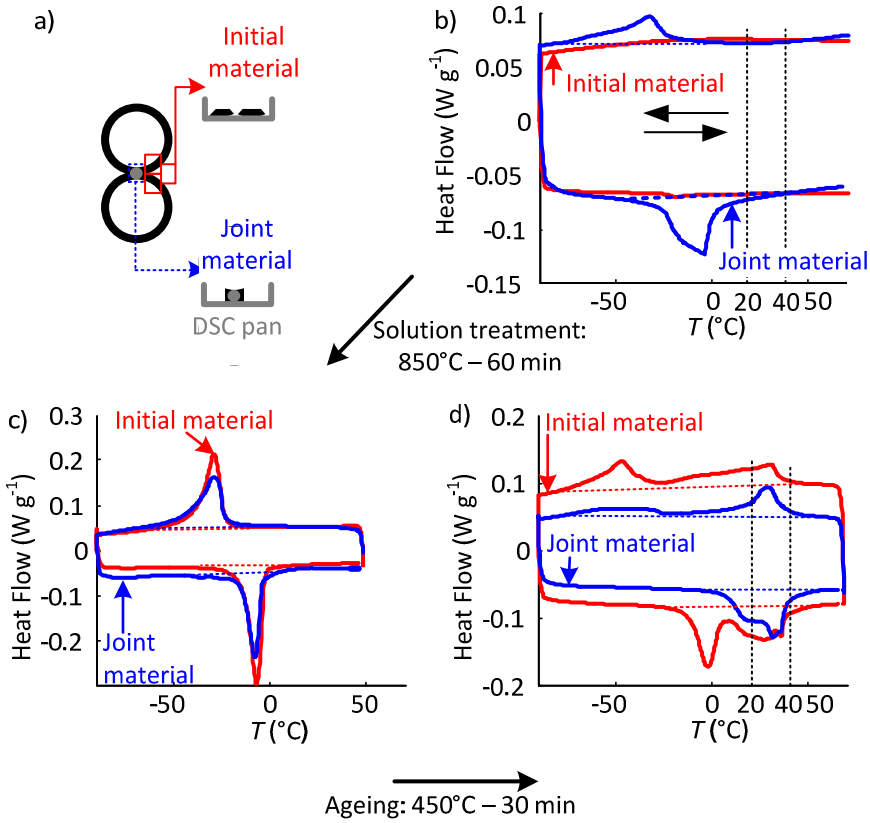

Figure 5: Transformation behaviour of welded samples: (a) Sample selection for DSC analysis. (b) As welded parts, (c) after solution treatment and (d) after ageing.

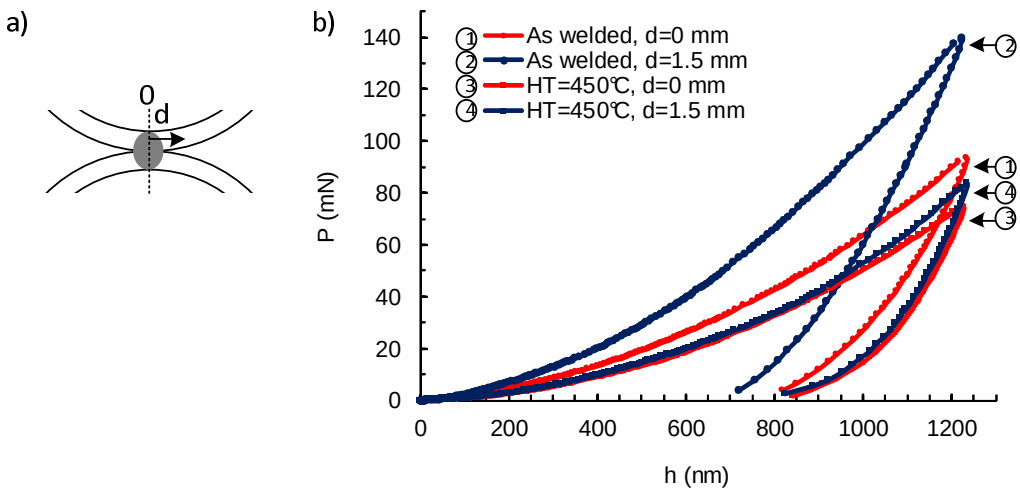

Figure 6: a) Definition of distance *d*. b) Nanoindentation curves of joint and initial material on as welded and on as welded and heat treated samples.

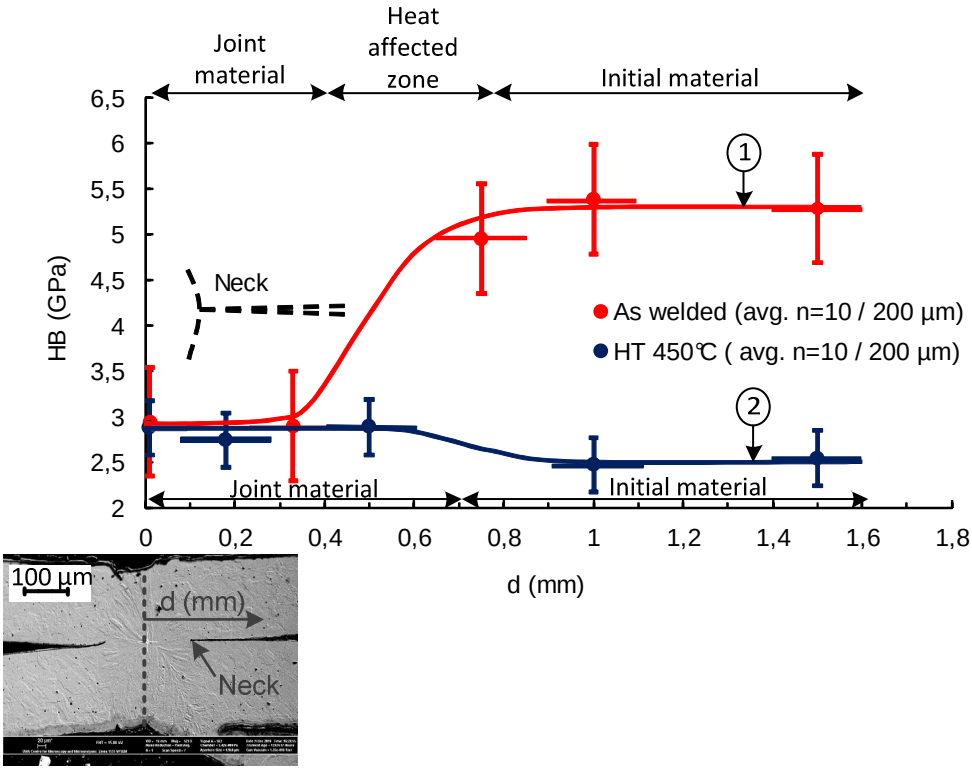

Figure 7: Hardness properties of as welded and heat treated structure.

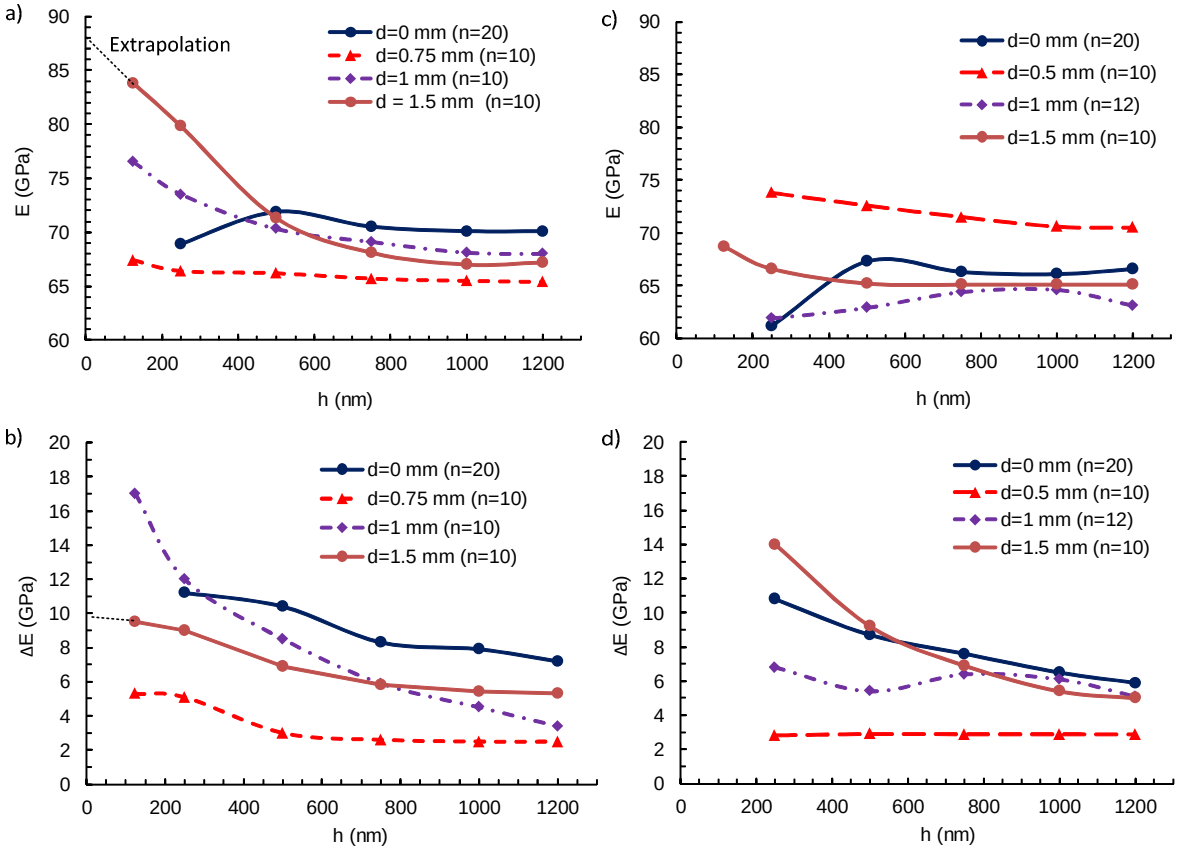

Figure 8: Nanoindentation measurement of Young's modulus of the tube material: (a) welded and (c) heat treated structure Indentation's modulus and (b),(d), respective associated measurement dispersion.

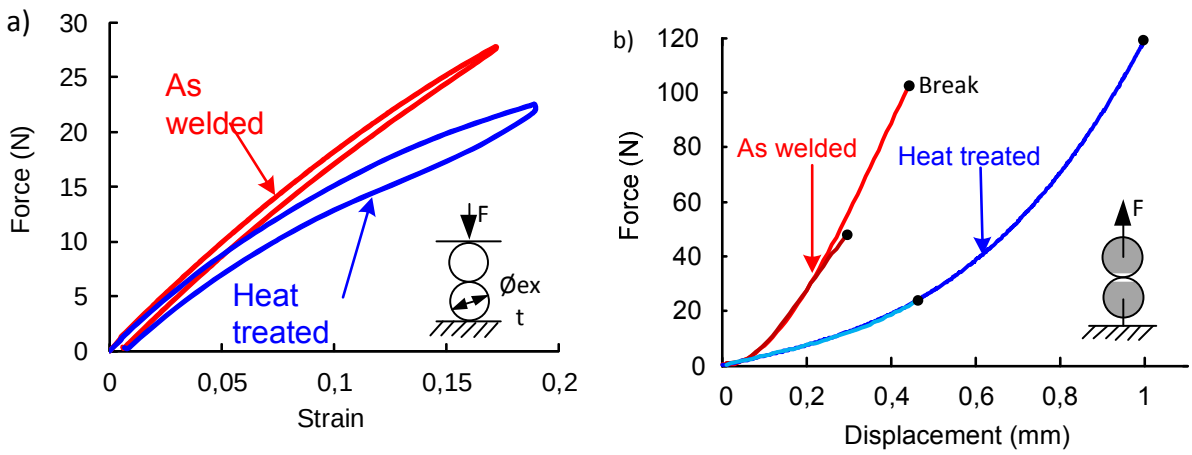

Figure 9: a) Compressive load-strain curves of twin-tubes samples in as welded and in heat treated states. b) Tensile load-displacement of twin-tubes in as welded and in heat treated states.